RSC Advances

PAPER

View Article Online
View Journal | View Issue

Cite this: *RSC Adv.*, 2025, **15**, 37673

Ratiometric photoluminescent sensing of 2,6-pyridinedicarboxylic acid using bimetallic metal–organic framework nanorods

Vu N. Doan, Hoang A. Vu, Le M. Dong, Vu H. Manh, Cao H. Thuong and Tran V. Thu *

Lanthanide-based metal–organic frameworks (MOFs) are promising probes for photoluminescent sensing of various chemical substances. In this study, we report the ultrasonication-assisted synthesis of bimetallic Eu/Tb-MOF nanorods for the highly sensitive detection of 2,6-pyridinedicarboxylic acid (DPA), a major biomarker for *Bacillus anthracis*. The prepared Eu/Tb-MOF nanorods exhibited a robust framework structure, uniform morphology, and strong photoluminescent emissions thanks to the synergy between Eu^{3+} and Tb^{3+} ions. The photoluminescent quenching effect is clearly observed upon the addition of DPA to these Eu/Tb-MOF aqueous suspensions, and has been utilized for sensing DPA. We achieved an impressive detection limit of 60 nM using the $Eu_{0.1}Tb_{0.9}BTC$ MOF with a low concentration of 20 mg L^{-1} in aqueous solvent, attributed to the unique energy transfer process from DPA to the Eu/Tb luminescent centers. The various factors which affect sensing performance including material system, lanthanide composition, DPA concentration, type of solvent and interferences were investigated. This work provides an efficient route for the synthesis of Eu/Tb-MOF nanorods as highly sensitive and selective photoluminescent sensors for DPA detection.

Received 30th May 2025
Accepted 28th September 2025

DOI: 10.1039/d5ra03817k

rsc.li/rsc-advances

1. Introduction

Bacillus anthracis (*B. anthracis*), the causative agent of anthrax, poses significant threats to public health and security due to its high morbidity and mortality rates.[1,2] This pathogen exists in two forms: as vegetative, rod-shaped cells under favorable growth conditions and as dormant spores when nutrients are limited. The spore form is particularly concerning because it can survive for decades and spread *via* contaminated food, water, or aerosolized particles, including those dispersed through ventilation systems, thereby posing risks to both animals and humans. Diagnosing anthrax is also challenging since the incubation period in humans can vary from 1 to 60 days, often delaying symptom onset. The remarkable resilience of *B. anthracis* spores is largely attributed to their multilayered protective structure, within which 2,6-pyridinedicarboxylic acid (DPA) serves as a major component, constituting about 5–15% of the dry mass.[3] Owing to its abundance and specificity, DPA has been widely recognized as a distinctive biomarker for anthrax spores, making its detection vital for early diagnosis and rapid response to potential exposure.[3]

Traditional methods for detecting DPA include chromatographic techniques and mass spectrometry.[4] While these methods offer high sensitivity and specificity, they often require sophisticated instrumentation and extensive sample preparation, and are not conducive to rapid, on-site analysis. Consequently, there is a pressing need for the development of simple, rapid, and sensitive detection methods for DPA.[5] Due to their low cost, quick reaction, and mobility, optical approaches for the detection of DPA have recently raised a lot of attention.[6,7] The recognition of biological substances has been investigated using surface plasmon resonance biosensors and surface enhanced Raman spectroscopy.[8]

Photoluminescence (PL) sensing has emerged as a promising approach for DPA detection due to its high sensitivity, selectivity, easy implementation, and potential for rapid and real-time analysis.[9] Lanthanide-based metal–organic frameworks (Ln-MOFs), which exhibit advantageous luminescence properties, including sharp/tunable emission bands and long luminescence lifetimes, are efficient photoluminescent materials.[10–13] Besides, these Ln-MOFs also offer various beneficial features, including large surface area, high porosity, and flexible structure thanks to the intrinsic nature of organic ligand–metal ion bonding. Recent studies have demonstrated the potential of europium (Eu^{3+}) and terbium (Tb^{3+})-based MOF PL sensors for the visual detection of DPA.[14] A monometallic Tb-MOF-based luminescent probe has been used for rapid detection of DPA in aqueous solution with LOD of 1.7 μM through an energy transfer mechanism.[15]

Faculty of Physics and Chemical Engineering, Le Quy Don Technical University, 236 Hoang Quoc Viet, Hanoi 100000, Vietnam. E-mail: thutv@mta.edu.vn; Tel: +84 964 793 732

The customizable design of Ln-MOFs is enabled to incorporate different types of both metal ions and organic ligands, which open avenues for exploratory research and applications, including PL sensing. Recently, bimetallic Ln-MOFs have gained worldwide interest due to their enhanced structural robustness, chemical stability, increased metallic sites, and high porosity for various potential applications.[16,17] As a result, bimetallic Ln-MOFs have shown superior advantages over monometallic Ln-MOFs in various applications. In the case of sensing application, the incorporation of both Eu^{3+} and Tb^{3+} ions into a single MOF can lead to synergistic effects, enhancing the material's luminescent properties and, consequently, its sensing performance.[6] Importantly, such a design concept enable ratiometric PL, a modern sensing technique that measures the ratio of emission intensities at two different wavelengths, rather than relying on a single PL signal.[3,14,18–20] This method provides more accurate and reliable results because it minimizes the effects of external factors such as probe concentration, environmental changes, and instrument fluctuations.[21] By monitoring the emission ratio between Tb^{3+} and Eu^{3+} ions within the bimetallic Ln-MOFs, the distinct and concentration-dependent changes in the Eu^{3+} and Tb^{3+} emission intensities upon DPA binding allow for precise and sensitive detection.

A series of mixed Eu/Tb-BTC (BTC = 1,3,5-benzenetricarboxylate) MOFs were synthesized by solvothermal method and dip-coated on indium-tin oxide glass to form a luminescent thin film for the sensing of pharmaceuticals.[22] The film emitted different luminescence with various intensity ratio of $^5D_0 \rightarrow {}^7F_2$ (Eu^{3+}, 619 nm) to $^5D_4 \rightarrow {}^7F_5$ (Tb^{3+}, 547 nm) transitions depending on the type and concentration of the guest pharmaceutical molecules. These luminescent signals are more stable and accurate than those based on single Eu-BTC MOFs. Bimetallic Tb_x/Eu_{1-x}BTC, prepared by wet grinding, shows strong red PL at 616 nm due to the energy transfer from Tb^{3+} to Eu^{3+}.[14] These transitions are blocked upon the introduction of DPA, because of the strong coupling between DPA (in the lowest triplet excited state, ^{3}DPA) and Tb^{3+} nodes. As a result, the PL turns to green at 544 nm, exhibiting an excellent correlation with DPA concentrations (50 nM to 3 μM) with a low detection limit of 4.9 nM. The wet grinding route is favour for scaling up, but hard to ensure a high degree of uniformity in particle size and morphology. The Tb/Eu@bio-MOF-1, prepared using organic solvent (DMF) requires high dosage (250 mg L^{-1}) for a limit of detection (LOD) of 34 nM.[19] The detection limits of $Tb_{0.9}Eu_{0.1}$(BTB)(DMF) and $Tb_{0.9}Eu_{0.1}$(BTB)(H_2O) for DPA are 78 nM and 240 nM, respectively.[3] Therefore, it is highly desired to develop greener synthetic route with better control over material properties for optimal sensing characteristics.

In this study, we adapted ultrasonication method to prepare a series of bimetallic Eu^{3+}/Tb^{3+}-MOFs from nitrate precursors. This novel, green and facile route also enable the formation of robust framework structures with uniform nanorods morphology, as confirmed by XRD, FT-IR, SEM, EDX, PL and UV spectroscopy. The PL properties of these bimetallic Eu/Tb MOF nanorods were thoroughly investigated, focusing on their selectivity and sensitivity toward DPA. We also examined various factors affecting the sensing performance, including the material system, lanthanide composition, DPA concentration, solvent type, and potential interferences. Our findings suggest that $Eu_{0.1}Tb_{0.9}$BTC nanorods hold significant promise as effective sensors for DPA detection in environmental and bioanalytical applications, offering a novel approach to the design of dual-emissive MOF-based sensors for practical PL sensing.

2. Experimental

2.1. Chemicals

Benzene-1,3,5-tricarboxylic acid (Trimesic acid, H_3BTC), methanol (CH_3OH), acetonitrile (CH_3CN), and tetrahydrofuran (C_4H_8O) were purchased from Shanghai Aladdin Bio-Chem Technology Co., Ltd. 2,6-Pyridine dicarboxylic acid ($C_7H_5NO_4$, PDA), europium(III) chloride hexahydrate ($EuCl_3 \cdot 6H_2O$), and terbium(III) chloride hexahydrate ($TbCl_3 \cdot 6H_2O$) were acquired from Macklin. Sodium acetate (CH_3COONa) was obtained from Xilong. All the chemicals used in this work are of analytical grade (content ≥ 99%) and used without further purification.

2.2. Material synthesis

2.2.1. Synthesis of Tb-BTC. Tb-BTC was synthesized by an adapted ultrasonication method.[23] First, $TbCl_3 \cdot 6H_2O$ (0.2024 g; 0.542 mmol), CH_3COONa (0.0164 g; 0.1 mmol) were dissolved in double-distilled H_2O (6 mL). Then, H_3BTC (0.2278 g; 1.084 mmol) and CH_3OH (8 mL) were added into the above solution and ultrasonicated for 30 min at 50 °C/40 kHz/407 W using a Daihan Scientific Ultrasonic Cleaner (Model WUC-D10H). The resulting powder was crystallized in a refrigerator, repeatedly washed with double distilled H_2O and CH_3OH, centrifuged, and dried at room temperature in a Petri dish to obtain Tb-BTC (yield: 31.4%).

2.2.2. Synthesis of $M_xTb_{1-x}(BTC)_n$. $M_xTb_{1-x}(BTC)_n$ MOFs (M = Eu, La, Ce, Pr, Nd; x = 0.1, 0.2, 0.3; n = 1, 2, 3) were also synthesized using the similar procedure. For example, for the synthesis of $Eu_{0.1}Tb_{0.9}$BTC (Fig. 1), $TbCl_3 \cdot 6H_2O$ (0.1825 g; 0.4887 mmol), CH_3COONa (0.0164 g; 0.1 mmol), $EuCl_3 \cdot 6H_2O$ (0.02 g; 0.0543 mmol) were dissolved in double-distilled H_2O (6 mL). Then, H_3BTC (0.2282 g; 1.086 mmol) and CH_3OH (8 mL) were added into the above solution and ultrasonicated for 30 min. The resulting powder (Product 1) was crystallized in a refrigerator to obtained Product 2, which was then repeatedly washed with double distilled H_2O and CH_3OH, centrifuged, and dried at room temperature in a Petri dish to obtain $Eu_{0.1}Tb_{0.9}$-BTC (yield: 36.7%). Table S1 shows the molar ratios of precursors used for the synthesis of $Eu_{0.1}Tb_{0.9}(BTC)_n$ (n = 1–3).

2.3. Material characterization

The crystal structures of all synthesized MOFs were determined by powder X-ray diffraction (XRD) on a Siemens D5005 diffractometer with Cu Kα radiation (λ = 0.15406 nm), scanning rate of 0.9°/min (scan step 0.03°), and 2θ ranging from 10 to 70°. Fourier transform infrared (FTIR) spectra were measured from 500 to 4000 cm^{-1} using a PerkinElmer Spectrum Two spectrometer equipped with a universal attenuated total reflectance

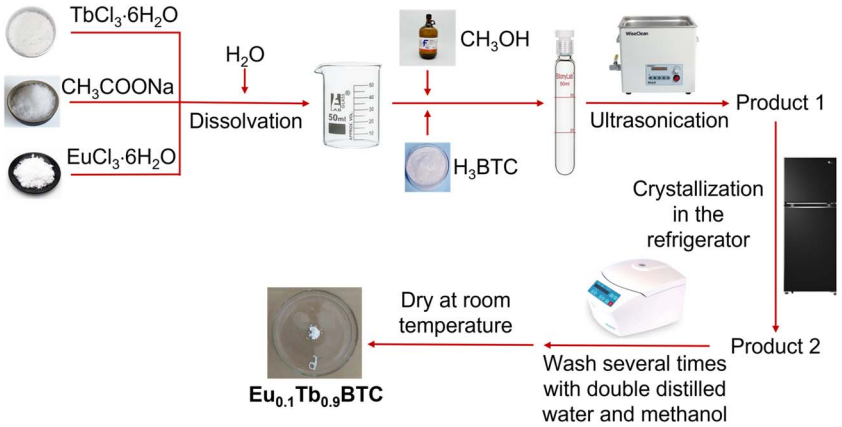

Fig. 1 Schematic synthesis of $Eu_{0.1}Tb_{0.9}BTC$.

accessory. The morphology of the prepared MOFs was obtained using scanning electron microscopy (SEM) on a Hitachi S-4800 field emission scanning electron microscope equipped with a Horiba EMAX energy-dispersive X-ray analyzer.

2.4. Photoluminescent determination of DPA

For DPA detection, the individual MOF (Tb-BTC or M_xTb_{1-x}(-BTC)$_n$) (1 mg each) was ultrasonicated for 30 min in 50 mL of double-distilled water at a concentration of 20 mg L^{-1}. Then, the calculated volumes of DPA solutions were added into the above solution to achieve desired concentrations (10^{-8} to 10^{-4} M). The obtained solutions were well shaken, and the PL spectra were measured with the excitation wavelength of 280 nm. The similar procedures were performed to investigate the influence of the $Eu_{0.1}Tb_{0.9}BTC$ concentrations, material system, lanthanide composition, type of solvent, and potential interferences.

3. Results and discussion

3.1. Materials characterization

The powder XRD patterns of the synthesized Tb-BTC and $M_{0.1}Tb_{0.9}BTC$ (M = Eu, La, Ce, Pr, and Nd) are shown in Fig. 2a. All observed diffraction peaks of the Tb-BTC can be well matched with the simulated patterns of $Tb(BTC)(H_2O)_6$ (CCDC #1499450),[24–26] as well as the known crystalline phases of $La(BTC)(H_2O)_6$,[27] Eu/Tb-doped $La(BTC)(H_2O)_6$,[28–30] $Eu(BTC)(H_2O)_6$,[31] Ln $(BTC)(H_2O)(DMF)_{1.1}$ (Ln = Tb, Dy, Er and Yb),[32] and $Tb_x/Eu_{1-x}BTC$[14] with monoclinic crystal structure and space group *Cc*. Major diffraction peaks were due to (110), (11−1), (021), (130), and (200) planes. In these isostructures, the trivalent lanthanide ions are nine-coordinated by three oxygen atoms from –COOH groups (of BTC ligands) and six oxygen atoms from coordinated water molecules. In $M_{0.1}Tb_{0.9}BTC$ MOFs, the lanthanide ions and terbium ions would randomly occupy the sites of lanthanide ions. Moreover, the presence of noncovalent interactions (hydrogen bonding and π–π interactions) results in the formation of a three-dimensional (3D) framework structure.[14] The peak positions are slightly shifted among the samples because of the different ionic sizes; however, the basic crystal structure was preserved, and no other side peaks are observed. Thus, the XRD patterns of $M_{0.1}Tb_{0.9}BTC$ (M = Eu, La, Ce, Pr, and Nd) demonstrate the successful synthesis of bimetallic MOFs by our ultrasonication-assisted method. The simulated crystal structure of Eu/Tb-BTC is presented in Fig. 2b.

The IR spectrum of H_3BTC shows characteristic bands of the carboxyl group of BTC ligands at 3090, 1720 and 537 cm^{-1} (Fig. 2c). These bands were not observed in Tb-BTC; instead, the valence vibrations of the asymmetric and symmetric carboxylic ions ($\nu_{as}(COO^-)$; $\nu_s(COO^-)$) were observed at 1556 and 1611 cm^{-1} (double peaks), 1435 cm^{-1}, and 1368 cm^{-1}. This was caused by the overlap of the ν_{as} vibrations of the surface acetate group and the backbone carboxylate group of BTC.[10] The peak at 516 cm^{-1} is the Ln–O valence vibration and the broad band at 3328 cm^{-1} is characteristic of the O–H group. The disappearance of the peak at 1720 cm^{-1} (of H_3BTC) is due to the complete deprotonation of the carboxylic acid and the coordination of the COO^- groups to Eu^{3+} and Tb^{3+} centers.[14]

SEM images of Tb-BTC and $Eu_{0.1}Tb_{0.9}BTC$ (Fig. 2d–f) display uniform, well-defined nanorod bundles with an average size of *ca.* 1–2 μm and highly crystalline structure. The formation of these nanostructures is directly related to the use of CH_3-COONa, which modulates the pH and coordination interactions between Eu/Tb and BTC ligands. Its presence helps to maintain a mildly basic environment, which facilitates deprotonation of the organic ligand and promotes coordination with metal ions during MOF formation. Additionally, it can influence the nucleation and growth kinetics, thereby affecting crystal size and morphology. The stoichiometric atomic percentages for C, O, Eu, and Tb are 56.25, 37.50, 0.63, and 5.63%, respectively. Whereas, the EDX-derived atomic percentages for C, O, Eu, and Tb in $Eu_{0.1}Tb_{0.9}BTC$ were 55.18, 39.57, 0.67, and 4.58%, respectively. EDX measurements for the $Eu_{0.1}Tb_{0.9}BTC$ (Fig. S1) revealed an Eu : Tb ratio of 0.67 : 4.58 ≈ 0.15; close to the stoichiometric value of 1 : 9 ≈ 0.1.

3.2. Excitation study of the Tb/Eu-BTCs

UV-Vis absorption, excitation, and PL spectra were measured to investigate the optical characteristics of $Eu_{0.1}Tb_{0.9}BTC$. As

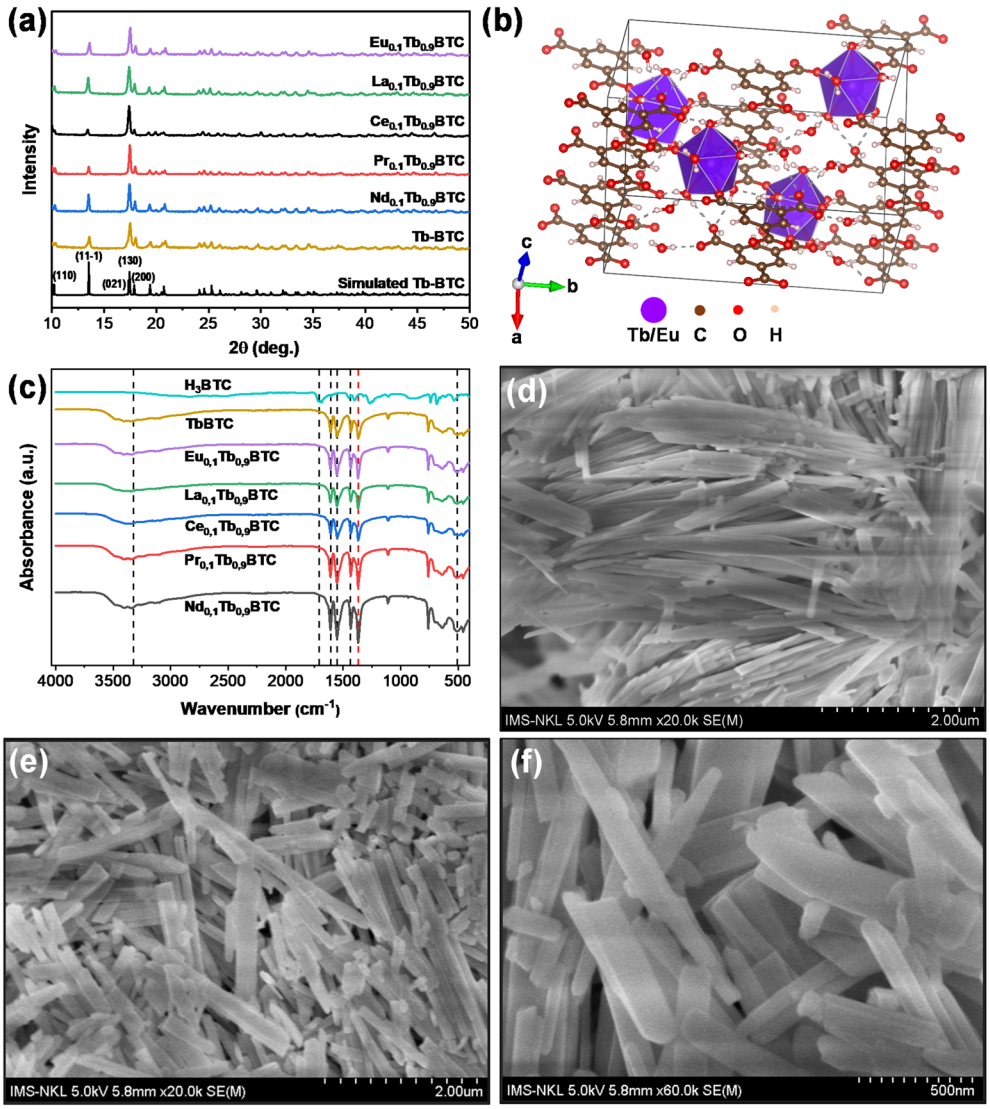

Fig. 2 (a) XRD patterns; (b) Simulated crystal structure of Eu/Tb-BTC; (c) FTIR spectra of Tb-BTC and $Ln_{0.1}Tb_{0.9}BTC$. SEM images of Tb-BTC (d) and $Eu_{0.1}Tb_{0.9}BTC$ (e and f).

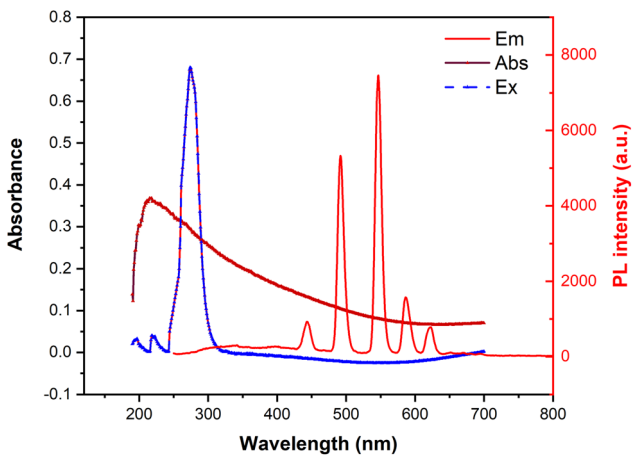

Fig. 3 UV-Vis absorption, PL excitation (λ_{em} = 619 nm) and PL emission (λ_{ex} = 280 nm) spectra of $Eu_{0.1}Tb_{0.9}BTC$.

shown in Fig. 3, the UV-Vis spectrum of $Eu_{0.1}Tb_{0.9}BTC$ has a broad range of absorption in the UV region, due to the π–π* transition on aromatic rings. The excitation spectrum of $Eu_{0.1}Tb_{0.9}BTC$, monitored at 546 nm, shows a broad band at 250–300 nm corresponding to ligand absorption, indicating efficient ligand-to-metal energy transfer and direct f–f transitions. The PL spectrum of $Eu_{0.1}Tb_{0.9}BTC$ displayed five PL emission peaks at *ca.* 446, 491, 546, 586, and 619 nm at the excitation wavelength of 280 nm. The peaks at 546 nm and 619 nm are dominant, indicating efficient PL from Eu^{3+} and Tb^{3+} centers at the chosen wavelength (280 nm). Hence, this wavelength was chosen for subsequent tests.

3.3. Selection of the MOF systems

For photoluminescent sensing, the MOFs with strong color change upon PL and having the lowest DPA detection limit are preferred. As seen, under an excitation wavelength (λ_{ex}) of

280 nm, the PL spectrum of Tb-BTC (black curve) displays four peaks at 491, 546, 586, and 622 nm, corresponding to characteristic $^5D_4 \rightarrow {}^7F_J$ emissions (J = 6, 5, 4, 3) of Tb^{3+} ions (Fig. 4a).[14] Among these, the strongest one at 586 nm matches with the $^5D_4 \rightarrow {}^7F_5$ emission. Upon adding DPA, the resulting PL spectrum (red curve) shows similar peaks of higher intensity, coincided with the intensification of the green PL of Tb-BTC (the inset in Fig. 4a).[33] Whereas, under the same λ_{ex}, the PL spectrum of Eu-BTC (black curve) displays four peaks at of 593, 619, 662, and 693 nm, corresponding to $^5D_0 \rightarrow {}^7F_J$ emissions (J = 1, 2, 3, 4) of Eu^{3+} ions (Fig. 4b).[14] Among these, the strongest one at 619 nm matches with the $^5D_0 \rightarrow {}^7F_2$ emission. The resulting PL spectrum when adding DPA (red curve) shows almost similar peak shape and intensity, demonstrated by the insignificant change of the pinkish-red color of Eu-BTC (the inset in Fig. 4b).

Since monometallic MOFs (Tb-BTC and Eu-BTC) exhibited poor color change upon adding DPA, multimetallic MOFs ($M_{0.1}Tb_{0.9}$BTC, M = Eu, Ce, La, Pr, Nd) were synthesized. Ce, La, and Nd were selected due to their potential roles in modifying the photophysical properties of the material: Specifically, Ce^{3+} is known to participate in energy transfer processes; La^{3+}, being optically inactive, was used as a structural diluent to investigate concentration effects; and Nd^{3+} was included for its near-infrared emission properties. Among these, the $Eu_{0.1}Tb_{0.9}$BTC best met the first criterion set above (Table S2). Its intrinsically red color turned to green when adding DPA, indicating an efficient energy transfer between $Eu_{0.1}Tb_{0.9}$BTC and DPA (the inset in Fig. 4c). This green color then diminished at higher concentrations of DPA, indicating photoluminescent quenching effect. As expected, the PL spectrum of $Eu_{0.1}Tb_{0.9}$BTC (black curve) displays all characteristic peaks of Tb^{3+} and Eu^{3+} ions (Fig. 4c). Upon adding DPA, the resulting PL spectrum (red curve) shows an increase in intensity at the PL peaks at 492 and 546 nm, well corresponding to $^5D_4 \rightarrow {}^7F_6$ and $^5D_4 \rightarrow {}^7F_5$ emission peaks of Tb^{3+} ions. Besides, the inital peak at 591 nm in $Eu_{0.1}Tb_{0.9}$BTC ($^5D_0 \rightarrow {}^7F_3$, Eu^{3+}) was also intensified and shifted to 588 nm ($^5D_4 \rightarrow {}^7F_4$, Tb^{3+}), due to greater contribution

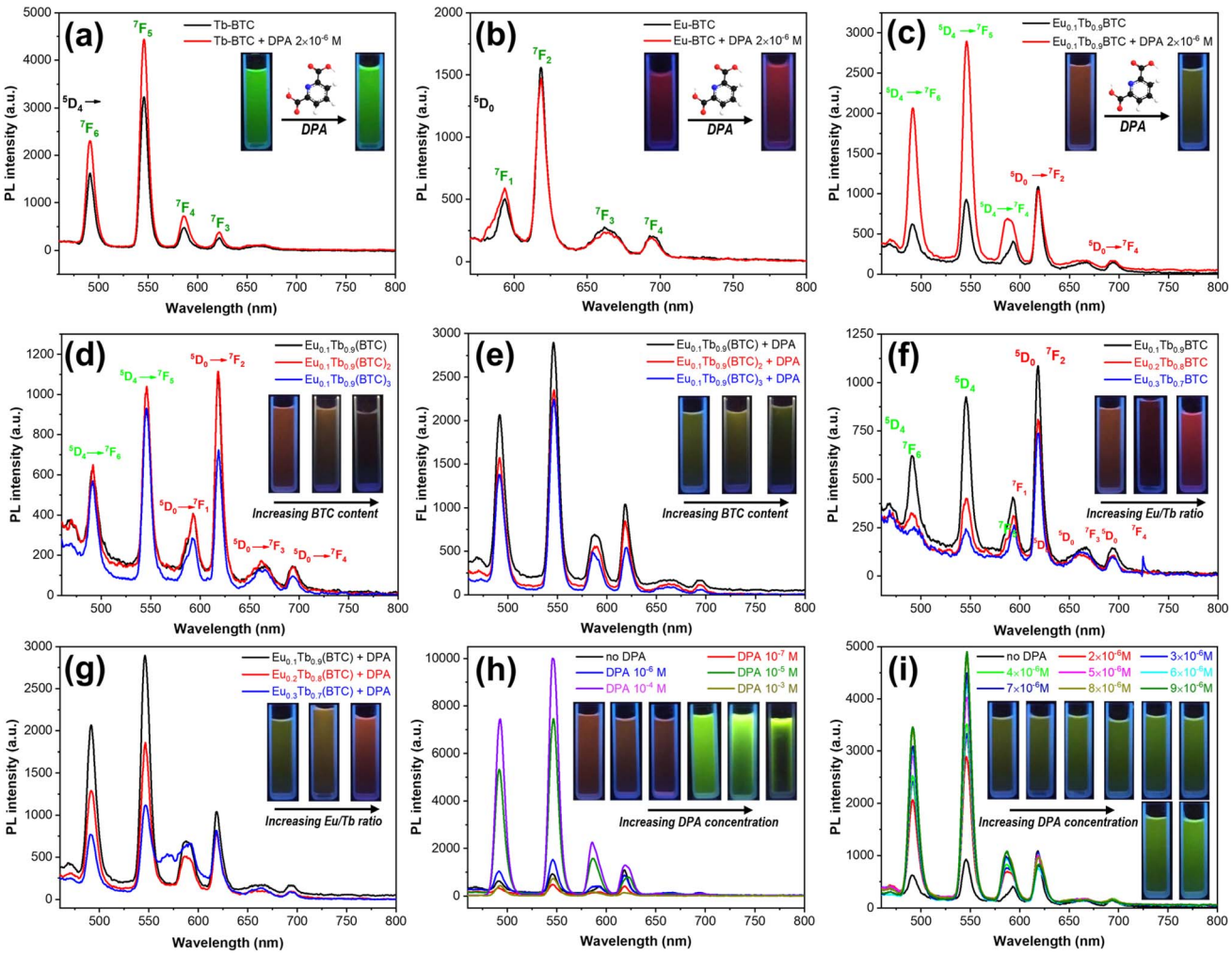

Fig. 4 PL spectra of Tb-BTC (a), Eu-BTC (b), $Eu_{0.1}Tb_{0.9}$BTC (c) before and after adding DPA. PL spectra of $Eu_{0.1}Tb_{0.9}(BTC)_n$ (n = 1,2,3) before (d) and after (e) adding DPA. PL spectra of Eu_xTb_{1-x}BTC (x = 0.1, 0.2, and 0.3) before (f) and after (g) adding DPA. PL spectra of $Eu_{0.1}Tb_{0.9}$BTC after adding DPA of different concentrations (h–i). The insets show PL of the corresponding solutions under a 254 nm UV lamp. Otherwise noted, the concentrations of MOFs were 20 mg L^{-1} and that of DPA was 2 × 10^{-6} M.

from Tb^{3+}–DPA interactions. Therefore, we chose $Eu_{0.1}Tb_{0.9}BTC$ for next investigations.

3.4. Influence of the solvent and the MOF system

The influence of different solvents (H_2O, CH_3OH, CH_3CN, and THF) on the PL property of $Eu_{0.1}Tb_{0.9}BTC$ was investigated. As shown in Fig. S2, the color change (after adding DPA) is most pronounced in the $Eu_{0.1}Tb_{0.9}BTC/H_2O$ solution. Whereas, $Eu_{0.1}Tb_{0.9}BTC/CH_3OH$ and $Eu_{0.1}Tb_{0.9}BTC/CH_3CN$ solutions exhibited a dim red color which remained little change with DPA concentration, and $Eu_{0.1}Tb_{0.9}BTC$/THF solution showed no PL when irradiated under an UV lamp. These effects suggest that the $Eu_{0.1}Tb_{0.9}BTC/H_2O$ solution has a lowest detection limit as compared to other ones, and thus met the second criterion set above. Thus, H_2O was chosen as the solvent for the following investigations. The PL effect for the other $M_{0.1}Tb_{0.9}BTC$/solvent solutions (M = La, Ce, Pr, and Nd) was also examined. As shown in Table S2, it was confirmed that the $Eu_{0.1}Tb_{0.9}BTC/H_2O$ solution exhibited the best metrics (clear color change) for DPA detection, and thus was chosen for subsequent studies.

3.5. Influence of the metal/ligand ratio

The metal/ligand atomic ratio in MOFs is an important factor which effects its sensing performance. In this study, a series of $Eu_{0.1}Tb_{0.9}(BTC)_n$ MOFs (n = 1, 2, and 3) were synthesized, whereas n was the input molar ratio between the BTC ligand and the total metal present. As seen in Fig. 4d, when n increases from 1 to 3, the intensity of the red PL of the MOFs became weaker. That is because, the red PL is regulated by $Tb^{3+} \rightarrow Eu^{3+}$ energy transfer,[14,23] and in MOFs with higher n, the Eu^{3+} percentage is smaller. The introduction of DPA interrupts this energy transfer and opens pathway for the characteristic red emission from Tb^{3+}, resulting in the transition of PL color from red to green, which occurs more quickly in $Eu_{0.1}Tb_{0.9}(BTC)_n$ with higher BTC content (Fig. 4e and S3). Here we chose the $Eu_{0.1}Tb_{0.9}BTC$ for the next studies, because its intrinsic red PL was clearer, and it also had a more obvious color change when DPA was added (although its green hue was not as intense as the other two remaining MOFs). In the PL spectra, the intensity of both red and green PL decreased with increasing n. However, while the intensity of red PL decreased sharply, the intensity of green PL decreased weaker, leading to the ratio of I_{546}/I_{619} increasing with increasing BTC content. As a result, the green color became more intense (and the red color also faded) with increasing BTC content when DPA was added.

3.6. Influence of the Eu/Tb ratio

The influence of Eu/Tb ratio on PL effect was investigated on three MOFs ($Eu_{0.1}Tb_{0.9}BTC$, $Eu_{0.2}Tb_{0.8}BTC$, and $Eu_{0.3}Tb_{0.7}BTC$). It was observed that when the Eu/Tb ratio increases, the intrinsic red PL of the corresponding MOF became more intense, but the green PL (emitted when DPA was added) occurred more slowly (Fig. 4f, g and S4), indicating lower sensitivity and potentially higher LOD towards DPA. This result means the higher the Eu percentage, the stronger the red PL, and the larger the amount of DPA is required to completely quenching the red PL (and "turn" the green PL on). The PL spectra also show that when increasing the Eu/Tb ratio, the emission peaks of Tb^{3+} ions decreased dramatically in intensity (*e.g.*, peak at 546 nm), while those of Eu^{3+} ions also decreased but with much lower degree. As a result, the I_{546}/I_{619} ratio decreased with increasing I_{546}/I_{619} ratio. Moreover, when increasing the Eu/Tb ratio, additional peaks at 662 and 619 nm were observed, which are the characteristic emission peaks of Eu^{3+} ions. Therefore, the $Eu_{0.1}Tb_{0.9}BTC$ was chosen for subsequent studies.

3.7. Influence of the concentration of $Eu_{0.1}Tb_{0.9}BTC$

$Eu_{0.1}Tb_{0.9}BTC$ aqueous solutions of different concentrations (100, 50, 30, 20, 15, 10, and 5 mg L^{-1}) were prepared for PL testings. Upon excitation at 280 nm UV light, the 100 mg L^{-1} $Eu_{0.1}Tb_{0.9}BTC$ solution exhibits a bright red color; the intensity of this red PL gradually decreases with decreasing concentration of $Eu_{0.1}Tb_{0.9}BTC$, and becomes very weak at 5 mg L^{-1} (Fig. S5). The concentration of 20 mg L^{-1} was selected for next studies because its color intensity is enough for convenient PL observation.

3.8. Influence of the concentration of DPA

The PL tests was performed using $Eu_{0.1}Tb_{0.9}BTC$ solutions with different concentrations of DPA (2×10^{-3}, 10^{-3}, 10^{-4}, 10^{-5}, 10^{-6}, 10^{-7}, and 10^{-8} M). The color change was not clearly visible at the DPA concentration of 10^{-8} M, but was more obvious at *ca.* 10^{-6} to 10^{-5} M (Fig. 4h and S6). When the DPA concentration was as high as 10^{-3} M, the color loss was observed due to the quenching effect. The intensity of characteristic emission peaks of Eu^{3+} ions decreases and that of Tb^{3+} increases with increasing DPA concentration up to 10^{-3} M, the value at which quenching effect comes into effect. Moreover, as a Lewis base, DPA can substitute coordinated water molecules to form $[Tb(DPA)]^+$ and $[Eu(DPA)]^+$ complexes that inhibit the energy transfer from Tb^{3+} to Eu^{3+}, enhance the emission of Tb^{3+} while suppress the emission of Eu^{3+}. However, at higher concentrations of DPA, Tb^{3+}–DPA bindings become dominate. As a result, the energy transfer between Tb^{3+} and BTC is inhibited, thus the characteristic emission of Tb^{3+} gradually decreases, similar to that observed in the Tb-BTC (quenching effect).[33] Therefore, the DPA concentrations range of 10^{-6} to 10^{-5} M was chosen for more in-depth investigations.

When the DPA concentration gradually increased from 2×10^{-6} to 9×10^{-6} M, a clear color change could be observed (Fig. 4i and S7). The red PL was no longer observed as at lower DPA concentrations (10^{-6}, 10^{-7}, and 10^{-8} M). Instead, the emitted PL gradually shifted to green color whose intensity increased with increasing DPA concentration from 10^{-5} to 10^{-4} M. It is thus concluded that the DPA concentration threshold that clearly changed the color of the $Eu_{0.1}Tb_{0.9}BTC$ system from red to green was from 2×10^{-6} to 10^{-5} M. As for the LOD, we examined DPA concentrations in the range from 2×10^{-8} to 6×10^{-8} M and found that at DPA concentration of 6×10^{-8} M, the red color of the material began to disappear. It is

thus concluded that the lowest detection limit of the $Eu_{0.1}Tb_{0.9}BTC$ material system with a concentration of 20 mg L^{-1} in aqueous solvent is 6×10^{-8} M DPA (60 nM) (Fig. S8).

In Fig. 5a, the I_{546}/I_{619} intensity ratio of the $Eu_{0.1}Tb_{0.9}BTC$ showed a linear correlation with DPA concentration in the range of 0.5–5.0 μM ($R^2 = 0.9906$), and the corresponding linear regression equation was $y = 0.5804C_{DPA} + 1.1929$. The calculated limit of detection (LOD) for DPA was 60 nM at a $Eu_{0.1}Tb_{0.9}BTC$ concentration of 20 mg L^{-1}, which was much below the infectious dosage of *B. anthracis* spores for human beings (60 μM).[19] Additionally, the CIE chromaticity diagram of $Eu_{0.1}Tb_{0.9}BTC$ (Fig. 5b) showed a considerable color shift after the addition of DPA, indicating the effectiveness for the visual assessment of DPA. As obviously shown, the addition of increasing concentrations of DPA ($0–2 \times 10^{-3}$ M) brought about a distinct and continuous shift in the chromaticity coordinates (x, y). The trajectory initiated in the red-orange region (due to the dominant Eu^{3+} emission at 619 nm in the absence of DPA), and proceeded through the yellow region towards the green area of the CIE diagram. This movement offers a quantitative correlation with the reduction of the BTC → Tb^{3+} → Eu^{3+} energy transfer pathway and the concurrent enhancement of direct DPA-sensitized Tb^{3+} emission at 546 nm.

3.9. Influence of the concentration of metallic ions

The influence of the concentration of metallic ions was examined in the presence of common metallic ions (chlorides) of the same concentration with DPA (8×10^{-6} M). It was found that, without DPA, the red PL of $Eu_{0.1}Tb_{0.9}BTC$ solutions remained minor change in the presence of Mg^{2+}, Ca^{2+}, Cu^{2+}, or Fe^{3+} ions, and showed significant change in the presence of Na^+ ions (Fig. S9). When DPA (8×10^{-6} M) was added into the above solution, the green PL of the ones containing Na^+, Mg^{2+}, or Ca^{2+} became slightly lighter than that of the DPA aqueous solution (of the same concentration); the solution containing Fe^{3+} showed the same color as at concentrations from 2 to 4 μM. Interestingly, the $Eu_{0.1}Tb_{0.9}BTC$ solution containing Cu^{2+} exhibited a red color, indicating the great influence of Cu^{2+} on DPA sensing performance. The sensitivity of $Eu_{0.1}Tb_{0.9}BTC$ towards DPA was reduced in the presence of Mg^{2+} or Ca^{2+}.

3.10. Influence of the pH

A systematic study on the pH-dependent luminescence behavior of the $Eu_{0.1}Tb_{0.9}BTC$ using CH_3COOH/NaOH buffer systems was conducted. As shown in Fig. 6a–c, the emission intensity of both Eu^{3+} and Tb^{3+} remained relatively stable within the pH range of 4.00 to 10.00, indicating that the probe performs reliably under near-neutral to moderately acidic/basic conditions. Within this range, the PL ratio also remained consistent, confirming that the presence of acetate ions does not significantly affect the luminescence properties. Beyond this optimal window, we observed clear pH-dependent variations. Under strongly acidic conditions (pH < 4.00), a gradual decrease in PL intensity was observed, with significant quenching at pH 3.00. Similarly, under alkaline conditions (pH > 10.00), both Eu^{3+} and Tb^{3+} emissions decreased sharply, with the Eu^{3+} emission showing slightly higher sensitivity to basic environments than Tb^{3+}. These results suggest that protonation and deprotonation of coordination sites may affect the ligand-to-metal energy transfer efficiency in extreme pH environments. Overall, these findings demonstrate that the $Eu_{0.1}Tb_{0.9}BTC$ maintains stable and effective luminescent performance within a practical working pH range of 4.00 to 10.00, which is suitable for most real-world sensing applications.

3.11. Selectivity study

The selectivity of the $Eu_{0.1}Tb_{0.9}BTC$ towards DPA was examined in the presence of organic acids isostructural to DPA (p-amino benzoic acid, phthalic acid, salicylic acid, and benzoic acid) of the same concentration with DPA (8×10^{-6} M). These organic acids are possible interfering analyte which might cause inaccurate sensing. The presence of p-amino benzoic acid, phthalic acid, and benzoic acid caused negligible changes to the PL of $Eu_{0.1}Tb_{0.9}BTC$ both before (red) and after adding DPA (green)

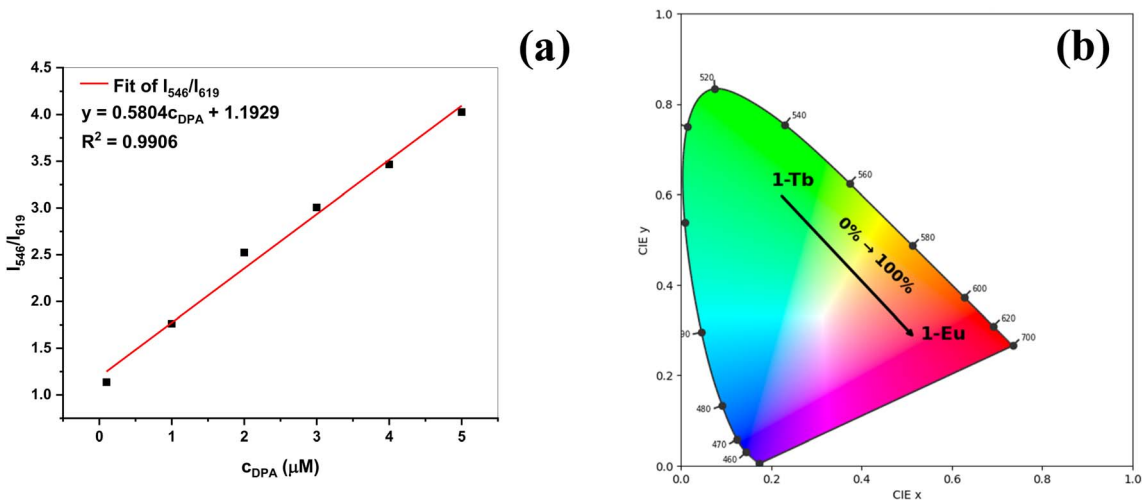

Fig. 5 (a) Plot of the emission intensity ratio (I_{546}/I_{619}) *versus* the DPA concentration. (b) The CIE chromaticity diagram of the $Eu_{0.1}Tb_{0.9}BTC$.

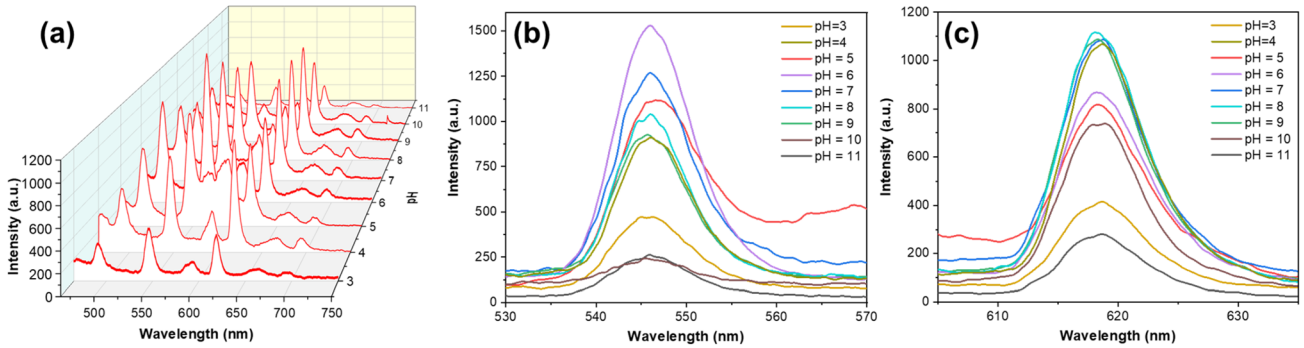

Fig. 6 (a) pH-dependent emission spectra of $Eu_{0.1}Tb_{0.9}BTC$ in the pH ranging from 3.00 to 11.00; (b) pH-dependent intensity of Tb^{3+} (546 nm) in the pH ranging from 3.00 to 11.00; (c) pH-dependent intensity of Eu^{3+} (619 nm) in the pH ranging from 3.00 to 11.00.

(Fig. S9). The only exception is salicylic acid, whose the presence turns the PL of $Eu_{0.1}Tb_{0.9}BTC$ pink (before adding DPA) and light green (after adding DPA). These results verified the high specificity of $Eu_{0.1}Tb_{0.9}BTC$ towards DPA.

3.12. Sensing mechanism

The luminescence lifetime decay profiles provide critical insights into the energy transfer (ET) processes governing the ratiometric PL response of $Eu_{0.1}Tb_{0.9}BTC$ toward DPA. As shown in Fig. 7, the addition of DPA induces a divergent effect on the lanthanide lifetimes: the Tb^{3+} emission at 546 nm ($^5D_4 \rightarrow {}^7F_5$) is prolonged from 256 to 293 μs, while the Eu^{3+} emission at 619 nm ($^5D_0 \rightarrow {}^7F_2$) is shortened from 253 to 197 μs. This opposing trend confirms that DPA modulates the ET pathway between Tb^{3+} and Eu^{3+} ions. The elongation of the Tb^{3+} lifetime suggests that DPA coordination displaces quenching water molecules from the Tb^{3+} coordination sphere, thereby suppressing non-radiative decay and enhancing green emission. In contrast, the reduced Eu^{3+} lifetime indicates inhibition of $Tb^{3+} \rightarrow Eu^{3+}$ transfer (ET2), as DPA competes with the BTC ligand for binding to Tb^{3+} and serves as a more efficient antenna for Tb^{3+} itself, thereby limiting population of the Eu^{3+} excited state. The simultaneous enhancement of Tb^{3+} emission and suppression of Eu^{3+} emission results in a pronounced ratiometric shift (I_{546}/I_{619}) and an observable color transition from red to green, which underpins the high sensitivity (LOD = 60 nM) and visual detection capability of the sensor. At elevated DPA concentrations, however, the initial sensitization is counteracted by dominant quenching mechanisms, including the inner filter effect (IFE) due to DPA absorption, MOF aggregation leading to enhanced non-radiative decay, and photoinduced electron transfer (PET) from the excited MOF to DPA, collectively accounting for the observed concentration-dependent emission suppression.

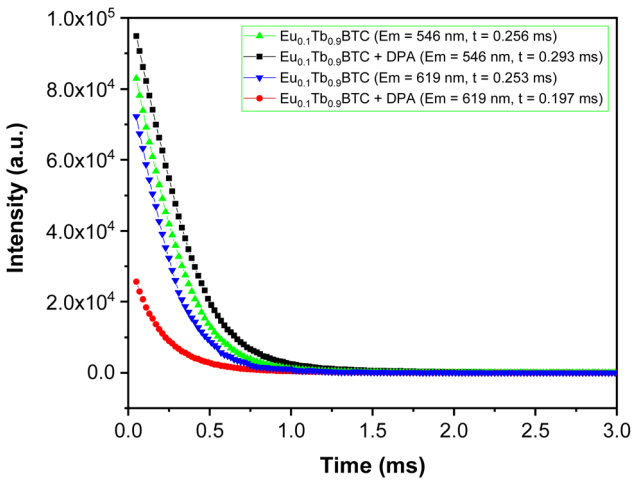

Fig. 7 Time-resolved PL decay of $Eu_{0.1}Tb_{0.9}BTC$ with and without DPA.

The DPA sensing mechanism through PL modulation can be rationalized by energy transfer considerations (Fig. 8).[14] Literature values place the lowest singlet (^{1}BTC) and triplet (^{3}BTC) excited states of H_3BTC at 32 465 cm^{-1} and 24 876 cm^{-1}, respectively, giving an energy gap of 7589 cm^{-1} that fulfills Reinhoudt's rule (>5000 cm^{-1}) and ensures efficient intersystem crossing. The energy difference between ^{3}BTC and the emitting level of Tb^{3+} (2500–4500 cm^{-1}) favors strong Tb^{3+} sensitization (ET1), whereas the mismatch with Eu^{3+} (optimal 2500–4000 cm^{-1}) leads to incomplete BTC $\rightarrow Eu^{3+}$ transfer. Nonetheless, efficient $Tb^{3+} \rightarrow Eu^{3+}$ energy transfer (ET2) accounts for the strong Eu^{3+} red emission at 619 nm, even in samples rich in Tb^{3+}. For DPA, the lowest triplet state (^{3}DPA) lies closer to the Tb^{3+} emitting level (ΔE = 5935 cm^{-1}) than Eu^{3+} (ΔE = 9115 cm^{-1}), enabling more effective DPA $\rightarrow Tb^{3+}$ transfer (ET3) but poor Eu^{3+} sensitization. In addition, DPA, acting as a Lewis base, can replace coordinated H_2O molecules and form $[Tb(DPA)]^+$ and $[Eu(DPA)]^+$ complexes, which not only suppress non-radiative decay but also disrupt the phonon-assisted Förster transfer from Tb^{3+} to Eu^{3+} (ET2). This dual effect enhances green Tb^{3+} emission while diminishing red Eu^{3+} emission, consistent with the observed ratiometric response. At higher DPA concentrations, however, excessive complexation and additional quenching pathways—including the inner filter effect, MOF aggregation, and photoinduced electron transfer—reduce the overall emission intensity, accounting for the concentration-dependent quenching behavior.

Previous reports also suggested the PL quenching of $Eu_{0.1}Tb_{0.9}BTC$ upon the addition of DPA can occurs by several

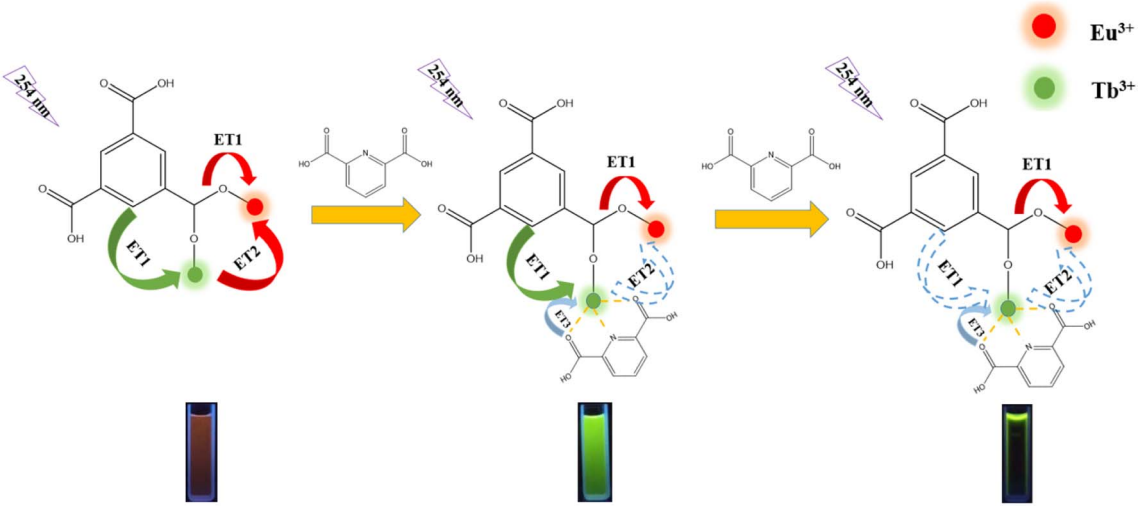

Fig. 8 PL photographs and quenching mechanisms of $Eu_{0.1}Tb_{0.9}$BTC. Energy transferred from BTC to Eu^{3+}/Tb^{3+} (ET1), from Tb^{3+} to Eu^{3+} (ET2), and from DPA to Tb^{3+} (ET3).

Table 1 Performance comparison of Ln-MOF photoluminescent sensors for DPA detection

Sensing probe method of synthesis	Probe concentration	LOD	Ref.
Eu-CDs	82.5 mg L^{-1}	10.6 nM	36
Tb-g-C_3N_4NS	8.3 mg L^{-1}	9.9 nM	37
$[Tb_4L_6(DMF)_5(H_2O)_3]\cdot 5DMF\cdot 6H_2O$ (H_2L = 5-[(anthracen-9-ylmethyl)-amino]-isophthalic acid)		1.7 μM	15
pSiNPs-Tb	10 mg L^{-1}	1.25 μM	38
$Tb_{0.875}Eu_{0.125}$-Hddb	666.6 mg L^{-1}	0.8494 μM	39
[Eu (DHBDC)$_{1.5}$(DMF)$_2$]·DMF	400 mg L^{-1}	1.3 μM	40
Tb(BTC)$(H_2O)_6$	—	0.04 nM	41
Tb/Eu@bio-MOF-1 solvothermal (DMF, H_2O)	250 mg L^{-1}	34 nM	19
$Tb_{0.875}Eu_{0.125}$-Hddb	2 mg/2.7 mL (HEPES)	849.4 nM	18
Eu-EBT/CDs	82.5 mg L^{-1}	10.6 nM	7
Wet-grinded $Tb_{0.4}/Eu_{0.6}$-BTC	20 mg L^{-1}	4.9 nM	14
$Tb_{0.9}Eu_{0.1}$(BTB)(DMF) $Tb_{0.9}Eu_{0.1}$(BTB)(H_2O)	—	78 nM	3
	—	240 nM	
$Eu_{0.1}Tb_{0.9}$BTC ultrasonication-assisted solvothermal	20 mg L^{-1}	60 nM	This work

pathways.[34] DPA's coordination to metallic sites or interaction with BTC disrupts the antenna effect, reducing energy transfer efficiency from the BTC ligand to metallic ions. In addition, DPA binding introduces vibrational modes (*e.g.*, from –OH or –COOH groups) that promote non-radiative relaxation of the excited Tb^{3+}, dissipating energy as heat rather than light. Furthermore, DPA may act as an electron acceptor, facilitating photoinduced electron transfer from the MOF, which competes with radiative emission. Also, if DPA absorbs light at the excitation or emission wavelengths of MOF, it can reduce the effective excitation light or reabsorb emitted light, contributing to quenching (inner filter effect).[35]

Table 1 compares the performance of several Ln-MOFs in photoluminescent sensing of DPA. The table explicitly highlighted some advantages of the $Eu_{0.1}Tb_{0.9}$BTC in our work, including green synthesis (using water as the only solvent), small probe concentration (20 mg L^{-1}), and high sensitivity (low LOD of 60 nM).

4. Conclusions

In summary, a series of bimetallic Eu^{3+}/Tb^{3+}-MOFs has been prepared by an ultrasonication-assisted route using water is the only solvent. The as-synthesized $Eu_{0.1}Tb_{0.9}$BTC nanorods possess robust framework structure, uniform morphology, and beneficial luminescent properties for DPA sensing. The photoluminescent quenching effect caused by complexing reaction between DPA and Eu^{3+}/Tb^{3+} centers was utilised to conveniently and reliably quantify DPA concentration. The influence of MOF system, lanthanide composition, DPA concentration, type of solvents and interferences were investigated and optimized. The LOD for DPA was 60 nM, achieved using the $Eu_{0.1}Tb_{0.9}$BTC with a low concentration of 20 mg L^{-1} in aqueous solvent, indicating high sensitivity and high selectivity. This work provides a green route for the synthesis of Eu/Tb-MOF nanorods as highly sensitive and selective photoluminescent sensors for DPA detection. Future works will focus on incorporating La-

MOF nanorods into solid-state optical devices for on-site detection.

Author contributions

Conceptualization, V. N. D.; methodology, all; formal analysis, all; writing-original draft preparation, V. N. D. and T. V. T.; writing-review and editing, T. V. T.; supervision, T. V. T. and V. N. D; funding acquisition, V. N. D.

Conflicts of interest

The authors declare no conflict of interest.

Data availability

Data are available from the corresponding author upon reasonable request.

Supplementary information is available. See DOI: https://doi.org/10.1039/d5ra03817k.

Acknowledgements

The authors acknowledge Le Quy Don Technical University for financial support (Project No. 2024.ĐH.04).

References

1 C. J. Carlson, I. T. Kracalik, N. Ross, K. A. Alexander, M. E. Hugh-Jones, M. Fegan, B. T. Elkin, T. Epp, T. K. Shury and W. Zhang, The global distribution of Bacillus anthracis and associated anthrax risk to humans, livestock and wildlife, *Nat. Microbiol.*, 2019, **4**, 1337–1343.

2 C. Lin and F. Zhigang, Modifying luminescent metal-organic frameworks with rhodamine dye: Aiming at the optical sensing of anthrax biomarker dipicolinic acid, *Inorg. Chim. Acta*, 2018, **477**, 51–58.

3 H.-M. Han, W.-W. Dong, M.-K. Li, D.-D. Xu, Z. Hu, J. Zhao and D.-S. Li, Ratiometric photoluminescence detection of an anthrax biomarker by modulating energy transfer in hetero Eu/Tb-MOFs, *Inorg. Chem. Commun.*, 2023, **153**, 110755.

4 T. Cecchi, S. Ferraro, F. Fusca, F. Pucciarelli and P. Passamonti, Determination of 2, 6-pyridinedicarboxylic acid in peach juice, *J. Liq. Chromatogr. Relat. Technol.*, 2000, **23**, 313–319.

5 K. F. Kayani, O. B. A. Shatery, S. J. Mohammed, H. R. Ahmed, R. F. Hamarawf and M. S. Mustafa, Synthesis and applications of luminescent metal organic frameworks (MOFs) for sensing dipicolinic acid in biological and water samples: a review, *Nanoscale Adv.*, 2025, **7**, 13–41.

6 S. S. Mohammed Ameen and K. M. Omer, Recent advances of bimetallic-metal organic frameworks: preparation, properties, and photoluminescence-based biochemical sensing applications, *ACS Appl. Mater. Interfaces*, 2024, **16**, 31895–31921.

7 Q. Zhou, Y. Fang, J. Li, D. Hong, P. Zhu, S. Chen and K. Tan, A design strategy of dual-ratiometric optical probe based on europium-doped carbon dots for colorimetric and photoluminescent visual detection of anthrax biomarker, *Talanta*, 2021, **222**, 121548.

8 H.-W. Cheng, W.-Q. Luo, G.-L. Wen, S.-Y. Huan, G.-L. Shen and R.-Q. Yu, Surface-enhanced Raman scattering based detection of bacterial biomarker and potential surface reaction species, *Analyst*, 2010, **135**, 2993–3001.

9 A. Krishna Mitra and N. Chakraborty, Advancing luminescent Sensing: Harnessing Metal-Organic frameworks for enhanced detection and analysis, *Inorg. Chim. Acta*, 2025, **578**, 122520.

10 H. Brunckova, E. Mudra, L. Rocha, E. Nassar, W. Nascimento, H. Kolev, A. Kovalcikova, Z. Molcanova, M. Podobova and L. Medvecky, Preparation and characterization of isostructural lanthanide Eu/Gd/Tb metal-organic framework thin films for luminescent applications, *Appl. Surf. Sci.*, 2021, **542**, 148731.

11 J. He, J. Xu, J. Yin, N. Li and X.-H. Bu, Recent advances in luminescent metal-organic frameworks for chemical sensors, *Sci. China Mater.*, 2019, **62**, 1655–1678.

12 S. S. Mohammed Ameen and K. M. Omer, Merging dual antenna effect with target-insensitive behavior in bimetal biligand MOFs to form efficient internal reference signal: color tonality-ratiometric designs, *ACS Mater. Lett.*, 2024, **6**, 2339–2349.

13 N. Sun, Y. Zhang, L. Yin, G. Xiong, L. You, Y. He and Y. Sun, A water-stable Tb-MOF as a multifunctional luminescent sensor for Fe^{3+} and $Cr_2O_7^{2-}$ in water, *Inorg. Chim. Acta*, 2023, **555**, 121581.

14 M. Wu, Z. W. Jiang, P. Zhang, X. Gong and Y. Wang, Energy transfer-based ratiometric photoluminescence sensing anthrax biomarkers in bimetallic lanthanide metal-organic frameworks, *Sens. Actuators, B*, 2023, **383**, 133596.

15 P.-P. Zhang, A.-Y. Ni, J.-J. Zhang, B.-L. Zhang, H. A. Zhou, H. Zhao, S. Liu, J. Ni and C. Duan, Tb-MOF-based luminescent recovery probe for rapid and facile detection of an anthrax biomarker, *Sens. Actuators, B*, 2023, **384**, 133624.

16 K. F. Kayani, Bimetallic metal–organic frameworks (BMOFs) for dye removal: a review, *RSC Adv.*, 2024, **14**, 31777–31796.

17 K. F. Kayani, Nanozyme based on bimetallic metal–organic frameworks and their applications: A review, *Microchem. J.*, 2025, **208**, 112363.

18 X.-B. Chen, C.-X. Qi, Y.-B. Xu, H. Li, L. Xu and B. Liu, A quantitative ratiometric photoluminescent Hddb-based MOF sensor and its on-site detection of the anthrax biomarker 2,6-dipicolinic acid, *J. Mater. Chem. C*, 2020, **8**, 17325–17335.

19 Y. Zhang, B. Li, H. Ma, L. Zhang and Y. Zheng, Rapid and facile ratiometric detection of an anthrax biomarker by regulating energy transfer process in bio-metal-organic framework, *Biosens. Bioelectron.*, 2016, **85**, 287–293.

20 S. S. Mohammed Ameen and K. M. Omer, Lanthanide and functionalization-free dual-state emitting zinc-based MOFs followed by dual-state detection: ratiometric and color-

tonality visual detection of tetracycline in solution and on paper in food and environmental samples, *Microchim. Acta*, 2024, **192**, 22.

21 L. Chen, D. Liu, J. Peng, Q. Du and H. He, Ratiometric photoluminescence sensing of metal-organic frameworks: Tactics and perspectives, *Coord. Chem. Rev.*, 2020, **404**, 213113.

22 Y. Gao, G. Yu, K. Liu and B. Wang, Luminescent mixed-crystal Ln-MOF thin film for the recognition and detection of pharmaceuticals, *Sens. Actuators, B*, 2018, **257**, 931–935.

23 J. Othong, J. Boonmak, F. Kielar, S. Hadsadee, S. Jungsuttiwong and S. Youngme, Self-calibrating sensor with logic gate operation for anthrax biomarker based on nanoscaled bimetallic lanthanoid MOF, *Sens. Actuators, B*, 2020, **316**, 128156.

24 W. Yang, J. Feng and H. Zhang, Facile and rapid fabrication of nanostructured lanthanide coordination polymers as selective luminescent probes in aqueous solution, *J. Mater. Chem.*, 2012, **22**, 6819–6823.

25 A. Gupta, M. Garg, S. Singh, A. Deep and A. L. Sharma, Highly Sensitive Optical Detection of Escherichia coli Using Terbium-Based Metal–Organic Framework, *ACS Appl. Mater. Interfaces*, 2020, **12**, 48198–48205.

26 M. Honjo, T. Koshiyama, Y. Fukunaga, Y. Tsuji, M. Tanaka and M. Ohba, Sensing of PLuoride ions in aqueous media using a luminescent coordination polymer and liposome composite, *Dalton Trans.*, 2017, **46**, 7141–7144.

27 Y. Wen, J. Cheng, Y. Feng, J. Zhang, Z. Li and Y. Yao, Synthesis and Crystal Structure of $[La(BTC)(H_2O)_6]_n$, *Chin. J. Struct. Chem.*, 2005, **24**, 1440.

28 K. Liu, G. Jia, Y. Zheng, Y. Song, M. Yang, Y. Huang, L. Zhang and H. You, Room-temperature synthesis and luminescence properties of Eu^{3+}/Tb^{3+}-doped La(1,3,5-BTC)$(H_2O)_6$, *Inorg. Chem. Commun.*, 2009, **12**, 1246–1249.

29 K. Liu, H. You, Y. Zheng, G. Jia, Y. Huang, M. Yang, Y. Song, L. Zhang and H. Zhang, Room-Temperature Synthesis of Multi-Morphological Coordination Polymer and Tunable White-Light Emission, *Cryst. Growth Des.*, 2010, **10**, 16–19.

30 K. Liu, Y. Zheng, G. Jia, M. Yang, Y. Song, N. Guo and H. You, Nano/micro-scaled La(1,3,5-BTC)$(H_2O)_6$ coordination polymer: Facile morphology-controlled fabrication and color-tunable photoluminescence properties by co-doping Eu^{3+},Tb^{3+}, *J. Solid State Chem.*, 2010, **183**, 2309–2316.

31 K. Liu, H. You, Y. Zheng, G. Jia, L. Zhang, Y. Huang, M. Yang, Y. Song and H. Zhang, Facile shape-controlled synthesis of luminescent europium benzene-1,3,5-tricarboxylate architectures at room temperature, *CrystEngComm*, 2009, **11**, 2622–2628.

32 A. Jamali, A. A. Tehrani, F. Shemirani and A. Morsali, Lanthanide metal–organic frameworks as selective microporous materials for adsorption of heavy metal ions, *Dalton Trans.*, 2016, **45**, 9193–9200.

33 I. Ahmed, H. J. Lee and S. Jhung, A Tb-based-metal–organic framework prepared under ultrasound for detection of organic amines in aqueous solution through photoluminescence quenching, *J. Mol. Liq.*, 2021, **344**, 117765.

34 X. Wang, Y. Jiang, A. Tissot and C. Serre, Luminescent sensing platforms based on lanthanide metal-organic frameworks: Current strategies and perspectives, *Coord. Chem. Rev.*, 2023, **497**, 215454.

35 S. Chen, Y.-L. Yu and J.-H. Wang, Inner filter effect-based photoluminescent sensing systems: A review, *Anal. Chim. Acta*, 2018, **999**, 13–26.

36 Q. Zhou, Y. Fang, J. Li, D. Hong, P. Zhu, S. Chen and K. J. T. Tan, A design strategy of dual-ratiometric optical probe based on europium-doped carbon dots for colorimetric and photoluminescent visual detection of anthrax biomarker, *Talanta*, 2021, **222**, 121548.

37 Y.-Y. Ma, Z.-J. Wang and D.-T. Qian, Ratiometric photoluminescence detection of anthrax biomarker based on terbium (III) functionalized graphitic carbon nitride nanosheets, *Talanta*, 2021, **230**, 122311.

38 Y. Jung, S. Kang, J. An, J. Jung and D. J. D. Kim, Porous silicon-based fluorescent nanoprobe for the detection of anthrax biomarker and its practical sensing applications, *Dyes Pigm.*, 2020, **182**, 108700.

39 X.-B. Chen, C.-X. Qi, Y.-B. Xu, H. Li, L. Xu and C. Liu, A quantitative ratiometric photoluminescent Hddb-based MOF sensor and its on-site detection of the anthrax biomarker 2, 6-dipicolinic acid, *J. Mater. Chem. C*, 2020, **8**, 17325–17335.

40 X.-Y. Zhao, J. Wang, H.-G. Hao, H. Yang, Q.-S. Yang and J. Zhao, A water-stable europium-MOF sensor for the selective, sensitive ratiometric photoluminescence detection of anthrax biomarker, *Microchem. J.*, 2021, **166**, 106253.

41 N. Bhardwaj, S. Bhardwaj, J. Mehta, K.-H. Kim and A. Deep, Highly sensitive detection of dipicolinic acid with a water-dispersible terbium-metal organic framework, *Biosens. Bioelectron.*, 2016, **86**, 799–804.